

# Design of a High–Resolution, High–Sensitivity PET Camera for Human Brains and Small Animals\*

W.W. Moses, *Senior Member, IEEE*, P.R.G. Virador, S.E. Derenzo, *Senior Member, IEEE*,  
R.H. Huesman, *Member, IEEE*, and T.F. Budinger, *Member, IEEE*  
Lawrence Berkeley National Laboratory, University of California, Berkeley, CA 94720

## Abstract

We present design parameters for a 3-D PET camera with high sensitivity (35 cm detector ring diameter, 15 cm axial field of view) and isotropic high resolution provided by detector modules capable of depth of interaction (DOI) measurement. Detector modules are made of LSO crystals (3 mm square by 30 mm deep) — the small module size and short decay time of LSO reduce the detector dead time by a factor of 14 compared to conventional BGO detector modules and narrow the coincidence window width to 4 ns. This yields an expected peak noise equivalent count rate of 800 kcps and noise equivalent sensitivity of 1370 kcps/ $\mu$ Ci/cc with a 20 cm diameter phantom — three to five times higher than conventional scanners. With 5 mm fwhm DOI resolution, the expected reconstructed spatial resolution is  $<3.0$  mm fwhm throughout the entire field of view. Depth of interaction measurement information is incorporated into the reconstruction algorithm by rebinning onto a regularly spaced grid. Attenuation correction is performed with an orbiting singles transmission source.

## I. INTRODUCTION

While the factors controlling the spatial resolution and efficiency of PET cameras have long been understood [1], performance limitations of 511 keV photon detectors force compromises into the design of practical PET imagers that prevent the fundamental limits of efficiency and resolution from being realized. As most 511 keV photon detectors utilize a common scintillator material (BGO), a common set of tradeoffs are imposed on PET camera designers resulting in similar PET camera designs. Incorporating LSO [2] scintillator into PET detector modules, which is becoming an increasingly realistic option, can significantly improve PET detector performance. The four-fold increase in light output and 7.5 times decrease in decay time change the set of compromises imposed on the PET camera designer and significantly alters the resulting camera design. We present herein a design study for one such camera that is predicted to obtain significantly higher spatial resolution and efficiency than present BGO based cameras, and hence should improve the quantitative accuracy and clinical utility of the reconstructed images.

The relevant scintillation properties of LSO and BGO are listed in Table 1. The main advantage of LSO over BGO is its

Table 1: Comparison of BGO and LSO scintillator properties.

	BGO	LSO
Chemical Formula	$\text{Bi}_4\text{Ge}_3\text{O}_{12}$	$\text{Lu}_2\text{SiO}_5:\text{Ce}$
Decay Time (ns)	300	40
Light Output (photons / MeV)	8,200	30,000
Attenuation Length (cm)	1.1	1.2
Photoelectric Fraction	43%	34%
Energy Resolution (511 keV)	10%	$<10\%$
Emission Wavelength (nm)	480	415
Index of Refraction	2.15	1.82
Radioactive Background?	No	Yes
Hygroscopic?	No	No

faster decay time, which allows a significant reduction in dead time and improvement in coincidence timing resolution. The higher light output of LSO allows development of depth of interaction measurement ability but (for reasons that are not understood) does not greatly improve the energy resolution.

## II. GENERAL TOMOGRAPH DESIGN

The design details for this high-sensitivity, high-resolution PET camera are summarized in Table 2. The patient port dimensions (30 cm diameter, 15 cm axial extent) are suitable for imaging the human brain, limbs, or small animals (such as dogs or monkeys), but too small to accommodate the human thorax. No space for inter-plane septa is provided so the camera can operate only in “fully 3-D” mode. The lack of septa allows a 35 cm detector ring diameter that is only slightly larger than the patient port. This reduces both the number of detector modules (and hence the cost) and the resolution degradation due to annihilation photon acollinearity. Reducing the diameter (while keeping the “standard” 15 cm axial extent) also increases the solid angle coverage, yielding a significant increase in sensitivity.

The detector requirements of this design exceed those of conventional cameras. Placing the detector modules closer to the patient port requires detectors with very high count rate performance to minimize dead time losses. The patient port nearly fills the detector ring, so severe radial elongation artifacts will be present unless the detector module can measure the interaction depth of individual 511 keV photons. The system is only capable of septaless operation, so good energy resolution is necessary to reject patient Compton scatter events and good timing resolution is necessary to reduce random coincidences. We believe that there are several LSO based design concepts that will soon provide 3 mm axial and transaxial crystal size, 6.25 cm<sup>2</sup> front surface area, 750 ps timing resolution, 20% fwhm energy resolution, and 10 mm fwhm

\*This work supported in part by the U.S. Department of Energy under Contract DE-AC-76SF00098, in part by the National Institutes of Health under grants P01-HL25840 and R01-NS29655.

Table 2. Comparison between a conventional PET camera and the proposed PET camera.

Quantity	Conventional Tomograph (ECAT EXACT HR [13])	Proposed Tomograph
Crystal size	5.9 mm x 2.9 mm x 30 mm	3 mm x 3 mm x 30 mm
Crystal material	Bi <sub>4</sub> Ge <sub>3</sub> O <sub>12</sub> (BGO)	Lu <sub>2</sub> SiO <sub>5</sub> :Ce (LSO)
Patient port diameter	56 cm	30 cm
Detector ring inner diameter	72 cm	35 cm
Block size	25 mm x 50 mm	25 mm x 25 mm
PMT size	25 mm x 25 mm (dual)	25 mm x 25 mm (single)
Crystals per block	56	64*
Blocks per ring	112	44
Number of Rings (15 cm axial FOV)	3	6
Blocks per system	336	264
Crystals per system	18,816	16,896*
PMTs per system	672 (dual anode)	264 (single anode)
Volume of scintillator crystal	12,600 ml (90 kg)	4,950 ml (37 kg)
Coincidence window width	12 ns	4 ns
Dead time per block	2.5 $\mu$ s	0.3 $\mu$ s
Maximum coincidence rate	1.4 MHz (ACS I)	10 MHz
Image resolution ( <sup>18</sup> F)	3.6 mm fwhm	2.2 mm fwhm*
Maximum noise equivalent event rate (in 20 cm dia. phantom)	2–D 110 k/s (at 2.0 $\mu$ Ci/cc) 3–D 90 k/s (at 0.4 $\mu$ Ci/cc)	2–D N/A 3–D 730 k/s (at 1 $\mu$ Ci/cc)

\* parameters that will change if the crystal size is other than 3 mm

DOI measurement resolution [3–7], so the this paper derives performance estimates based on these detector parameters.

This design shares the small ring diameter and lack of septa with the NaI(Tl) based PENN-PET camera [8], but the thicker scintillator and higher count rate capability allow our design to more fully utilize the increased solid angle coverage, resulting in significantly increased sensitivity. The BGO based ECAT EXACT3D camera [9] has a septaless design and thick scintillator crystal, but the depth of interaction capability in our design allows the detector diameter to be reduced substantially without degrading spatial resolution, yielding equivalent solid angle coverage and higher spatial resolution with significantly less detector material. While it could be used to image smaller animals (such as rats or mice), the cost and performance for this task would not be as favorable as for cameras specifically designed for this purpose [10–12].

### III. PERFORMANCE ESTIMATES

#### A. Spatial Resolution

The contributions to spatial resolution near the center of a tomograph with adequate sampling are the crystal size, crystal decoding process, annihilation photon acollinearity, positron range, and reconstruction algorithm. A reasonably accurate estimate of the reconstructed image resolution (fwhm) of an arbitrary PET camera can be made using the formula

$$= 1.25 \sqrt{(d/2)^2 + (0.0022D)^2 + R^2 + b^2}, \quad (1)$$

where  $d$  = detector width,  $D$  = detector cylinder diameter,  $R$  = effective positron range, and  $b$  is a factor due to the crystal decoding process (0 if the crystal of interaction is individually coupled to a photodetector and 2.2 otherwise), with units of millimeters for all quantities. The  $b$  factor, while empirically determined for BGO detector modules, has been found to be

necessary to “predict” the performance of several new high resolution PET cameras [14].

With the design proposed, the crystal width is 3.0 mm, the detector ring diameter is 350 mm, and the crystals would preferably be individually coupled to photodetectors. This yields contributions of 1.5 mm for crystal size, 0.8 mm for acollinearity, and 0 mm for crystal decoding. When imaging <sup>18</sup>F ( $R=0.5$  mm), a reconstructed spatial resolution of 2.2 mm is predicted, while a design with 2.0 mm square crystals would yield 1.8 mm fwhm resolution.

#### B. Radial Elongation

The spatial resolution predicted by Equation 1 applies only near the center of the tomograph (*i.e.* distances less than 10% of the ring diameter), where penetration of 511 keV photons into adjacent crystals is minimal and radial elongation is not present. Measuring the interaction depth on an event by event basis can significantly reduce this elongation; the amount of reduction depends both on the detector ring diameter and the resolution with which the interaction depth is measured.

To predict the spatial resolution for a single plane PET camera with 3 mm LSO crystals, a Monte Carlo simulation is performed. This simulation assumes the detector module design in [6], and includes annihilation photon acollinearity, energy dependent Compton and photoelectric cross sections, and finite (20% fwhm at 511 keV) detector energy resolution, with the measured interaction depth assumed to be the true interaction depth blurred by a Gaussian with fixed width. If Compton interactions cause energy to be deposited in more than one crystal, the crystal with the higher energy is assigned as the crystal of interaction, and if there are multiple energy depositions in a single crystal, the true position is assumed to be the center of gravity of the energy depositions. Data are reconstructed with filtered backprojection with the depth of

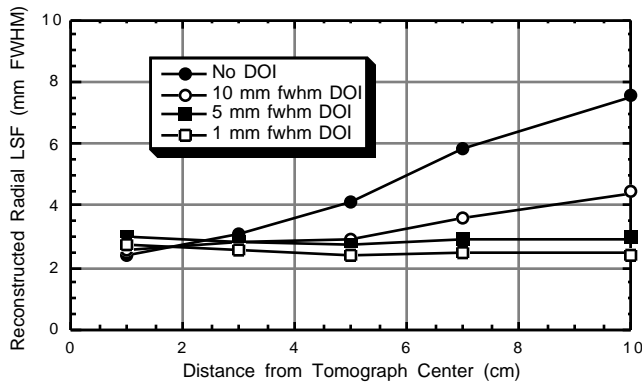


Figure 1: The radial component of the reconstructed point spread function as a function of position from the tomograph center, for several depth of interaction measurement resolutions. The scintillator crystals modeled are 3 mm square by 30 mm long.

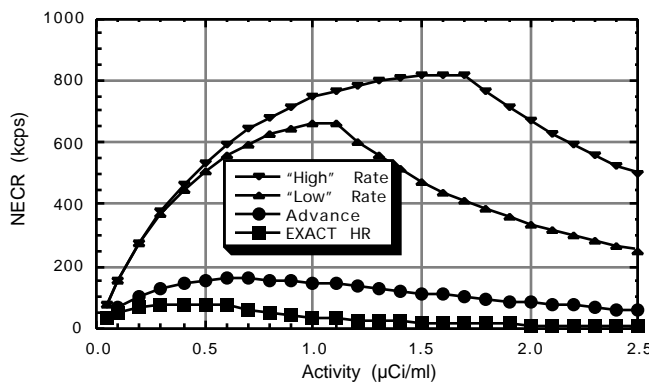


Figure 2: The noise equivalent count rate (NECR) versus activity concentration in a 20 cm diameter phantom for several tomograph designs.

interaction information incorporated by the rebinning algorithm described in Section IV-B.

The results of this simulation are shown in Figure 1, which plots the full width at half maximum (fwhm) of the reconstructed line source image (in the radial direction) as a function of distance from the tomograph center. Tomographs with several different depth of interaction (DOI) measurement resolutions are simulated. Without DOI information, the familiar radial elongation artifact degrades the spatial resolution by a factor of 3 at a distance of 10 cm from the tomograph center. However, this affect is significantly reduced even with 10 mm fwhm DOI measurement resolution, which is relatively easily obtained. With a DOI measurement resolution of 5 mm fwhm (which is obtainable, though with greater difficulty) the spatial resolution becomes essentially uniform at 2.5–3.0 mm fwhm throughout the field of view. Similar simulations were performed with 30 cm and 40 cm detector ring diameters, and the predicted spatial resolution is insensitive to ring diameter.

### C. Noise Equivalent Count Rate

The small ring diameter, septaless operation, and the low dead time of LSO give this design an extremely high efficiency. A measure of a PET camera's capability to accurately

image activity in the field of view is the noise equivalent count rate (NECR) [15]. The NECR for a 20 cm diameter water filled phantom is estimated with an analytic computation that includes dead time in the front end and coincidence processing electronics, scatter and attenuation in the phantom, and the effects of energy discrimination in the detector modules. Scatter subtraction is not explicitly performed; the number of scatter events is assumed to be a fixed fraction of the true coincidence events. This fraction is determined by Monte Carlo simulation to be 75% for an 85 cm diameter ring and 120% for a 35 cm diameter ring. To validate this analysis, we compare the computed NECR versus activity concentration to published values for the CTI/Siemens ECAT EXACT HR [13] and the GE Advance [16] operated in septaless mode. The predicted curves, plotted in Figure 2, agree with the published data to within 10%. The data in Figure 2 does not necessarily represent present capabilities of these manufacturers, but is used only to validate the analysis.

Figure 2 also shows the computed NECR versus activity concentration for the proposed detector assuming a 35 cm detector diameter. Two sets of assumptions for dead time are modeled — a low rate design (that assumes a 300 ns detector dead time and a 10 MHz coincidence processing limit) and a high rate design (that assumes a 200 ns detector dead time and a 20 MHz coincidence processing limit). A maximum NECR of 700–800 kcps is obtained with activity densities of 1.0–1.5  $\mu\text{Ci/ml}$ . Thus, the proposed design has roughly a factor of five higher peak NECR than either of these existing scanners, mostly due to its lower dead time, high coincidence processor throughput, and narrow (4 ns) coincidence window.

Similar computations predict that increasing the ring diameter to 40 cm increases the NECR approximately 10%, while reducing the diameter to 30 cm decreases the NECR approximately 40%. These differences in NECR are mostly due to significant differences in the randoms rate. With a 30 cm diameter patient port, 100% of the possible detector module pairs in a 30 cm diameter detector ring form valid coincidences, while only 54% of the possible detector pairs form valid coincidences with a 40 cm diameter detector ring. The singles rate is nearly independent of ring diameter, so the randoms rate is roughly proportional to the fraction of detector module pairs that form valid coincidences.

### D. Noise Equivalent Sensitivity

A measure of a PET camera's efficiency for detecting activity in the field of view is the noise equivalent sensitivity (NES) [17], which is the slope of the NECR versus activity density curve at zero activity density. The NES of this design is predicted to be 1370 kcps/ $\mu\text{Ci/cc}$  — the same analytic computation obtains an accurate NES for the CTI/Siemens ECAT EXACT HR (710 kcps/ $\mu\text{Ci/cc}$ ) and the GE Advance (770 kcps/ $\mu\text{Ci/cc}$ ) operated in septaless mode. Thus, the NES of the proposed design is approximately two times higher than existing designs. This factor is attributed to the increased solid angle — the reduced random event contribution enabled by the narrow coincidence window is canceled by the increased scatter

fraction contribution due to the larger solid angle coverage. The 4 ns coincidence window in this design comfortably accommodates the expected 2 ns time of flight difference across the detector ring and 1 ns fwhm coincidence time resolution.

#### IV. ADDITIONAL CONSIDERATIONS

##### A. Attenuation Correction

The lack of inter-plane septa (and hence the inability to take any data in 2-D mode) makes attenuation correction difficult, as attenuation maps for 3-D reconstruction are usually derived from transmission scans taken in 2-D mode. We anticipate following the lead of other groups and using a high activity point source that emits 662 keV photons to perform transmission measurements [18, 19]. While such data have a higher scatter contamination than data collected with windowed coincidence sources, the relatively uniform attenuation coefficient in the human head and low attenuation and scatter fraction in small animals are likely to minimize the effect.

##### B. Including Depth of Interaction Information

Previous reconstruction algorithms [20] have incorporated depth of interaction measurement information in the following manner. A line is constructed joining the measured interaction points, and the  $r$  and  $\theta$  values of the resulting chord computed. This event is then assigned to the nearest “physical” chord, where a “physical” chord is defined to be a line connecting the center of the front faces of two crystals. Due to the circular shape of the tomograph ring, these “physical” chords become more closely spaced in  $r$  as they move away from the center of the tomograph. This change in spacing is more pronounced for our design than for conventional PET cameras, as the patient port diameter fills a significantly larger fraction of the detector ring diameter. As conventional reconstruction algorithms use evenly spaced bins, the “physical” chords are then interpolated onto a grid of evenly spaced “ideal” chords, which are then reconstructed with filtered backprojection.

We propose a variant of this rebinning algorithm where the line joining the measured interaction points is assigned directly to the “ideal” chord. This obviates the interpolation to “physical” and then to “ideal” chords. The chord spacing in  $r$  need not be constrained to half the detector width ( $d/2$ ), and so a smaller spacing (e.g.  $d/4$ ) can be used to improve the radial sampling and so the reconstructed spatial resolution. For chords that pass near the center of the tomograph, some interpolation is necessary to avoid unfilled chords, and subsequent normalization (performed in the same way as with conventional scanners) is necessary to avoid aliasing artifacts caused by the nonuniform sampling. It is possible that rotating the detector modules slightly so that their front faces are not normal to the line connecting them to the tomograph center [21] could avoid unfilled chords, but the other ramifications of this approach have not been explored.

The left hand image in Figure 3 shows a point source located 10 cm from the center of the tomograph, reconstructed using the above algorithm. The data were simulated using the

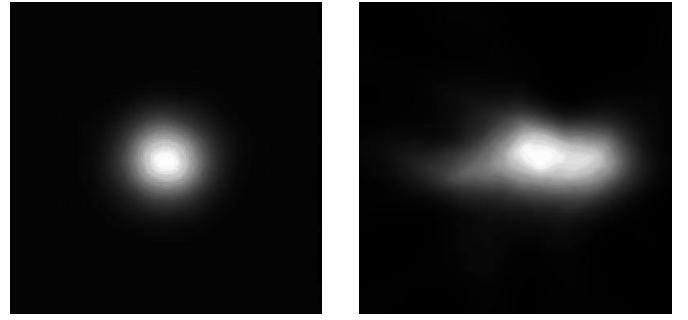


Figure 3: The image of a point source displaced 10 cm horizontally from the center of the tomograph, reconstructed with the rebinning algorithm described herein. The image at left is with 5 mm fwhm DOI measurement resolution, the image at the right is without DOI information. The field of view is 1 cm square.

Monte Carlo described in Section III-B with 3x3x30 mm crystals, a 35 cm diameter detector ring, and 5 mm fwhm DOI measurement resolution, and the data reconstructed in 2-D with a ramp filter. The image is free of artifacts from penetration of 511 keV photons in the detector ring or from the reconstruction algorithm, and the point spread function is 3.0 mm fwhm in the radial direction and 2.9 mm fwhm in the tangential direction. The image at the right includes no DOI information, and shows severe radial elongation artifacts. Figure 1 shows the expected reconstructed spatial resolution as a function of DOI measurement resolution. This algorithm also produces artifact free images of extended source phantoms.

While the above images are reconstructed with a 2-D algorithm, the concepts for including depth of interaction measurement information and directly rebinning onto a regularly spaced grid can be extended to 3-D reconstruction algorithms. The lines of response from a cylindrical tomograph are actually neither evenly spaced nor parallel; the transverse separation of the lines decreases and the elevation angles of the lines increase with distance from the central axis of the cylinder as shown in Figure 4. The rebinning onto a regularly spaced

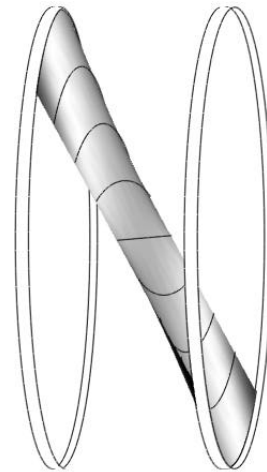


Figure 4: Geometric lines of response from oblique (cross-plane) slices. Deviation from parallel, coplanar lines is apparent, and is caused by connecting arc segments rather than line segments. Current 3-D reconstruction algorithms ignore this effect.

grid will be applied to both the in-plane ( $r, \theta$ ) and cross-plane ( $\phi$ ) coordinates, eliminating the geometrical errors caused by non-uniform sampling in both the  $r$  and  $\phi$  directions. This rebinning would be performed before the data are histogrammed (or the data could be taken in list mode) so the number of chords that are backprojected is similar to that of a conventional 3-D scanner. This implies that although the address defining a single crystal must contain three additional bits (for depth of interaction information) and the coincidence processor must be more sophisticated in order to perform this rebinning, no additional memory is necessary.

## VI. CONCLUSIONS

A conceptual design is presented for a PET camera designed to image the human brain and small animals. Removing the interplane septa and reducing the detector ring diameter so that it is slightly larger than the field of view affords a dramatic increase in solid angle coverage compared to conventional PET cameras and reduces the number of detector modules significantly, potentially reducing the cost. Using LSO scintillator material in the detector modules results in low dead time, which coupled with high coincidence processor throughput allows the increased solid angle coverage to be converted into a significantly increased noise equivalent count rate. The detector modules must be able to measure the depth of interaction on an event by event basis in order to eliminate radial elongation artifacts, but such depth information can be incorporated into the reconstruction algorithm in an artifact free way with a simple rebinning method.

## VII. ACKNOWLEDGMENTS

This work is supported in part by the Director, Office of Energy Research, Office of Health and Environmental Research, Medical Applications and Biophysical Research Division of the U.S. Department of Energy under contract No. DE-AC03-76SF00098, in part by the Public Health Service grants No. P01-HL25840 and No. R01-NS29655, awarded by the National Heart, Lung, and Blood Institute, and the Neurological Disorder and Stroke Institute, Department of Health and Human Services.

## VIII. REFERENCES

- [1] S. E. Derenzo, "Recent developments in positron emission tomography (PET) instrumentation," in *Physics and Engineering of Computerized Multidimensional Imaging and Processing*, vol. SPIE Vol. 671, *Physics and Engineering of Computerized Multidimensional Imaging and Processing*, O. Nalcioglu, Z. H. Cho, and T. F. Budinger, Eds., 1986, pp. 232–243.
- [2] C. L. Melcher and J. S. Schweitzer, "Cerium-doped lutetium orthosilicate: A fast, efficient new scintillator," *IEEE Trans. Nucl. Sci.*, vol. NS-39, pp. 502–504, 1992.
- [3] C. Moisan, G. Tsang, J. G. Rogers, et al., "Performance studies of a depth encoding multicrystal detector for PET," *IEEE Trans. Nucl. Sci.*, vol. NS-43, pp. 1926–1931, 1996.
- [4] W. Worstell, O. Johnson, and V. Zawarzin. Development of a high-resolution PET detector using LSO and wavelength-shifting fibers. *Proceedings of The IEEE Nuclear Science Symposium and Medical Imaging Conference*, pp. 1756–1760, (Edited by P. A. Moonier), San Francisco, CA, 1995.
- [5] W. W. Moses, S. E. Derenzo, C. L. Melcher, et al., "A room temperature LSO / PIN photodiode PET detector module that measures depth of interaction," *IEEE Trans. Nucl. Sci.*, vol. NS-42, pp. 1085–1089, 1995.
- [6] J. S. Huber, W. W. Moses, S. E. Derenzo, et al., "Characterization of a 64 channel PET detector using photodiodes for crystal identification," *IEEE Trans. Nucl. Sci.*, vol. NS-44, (in press), 1997.
- [7] M. E. Casey, L. Eriksson, M. Schmand, et al., "Investigation of LSO crystals for high spatial resolution positron emission tomography," *IEEE Trans. Nucl. Sci.*, vol. NS-44, (in press), 1997.
- [8] R. J. Smith, J. S. Karp, and G. Muehllehner, "The countrate performance of the volume imaging PENN-PET scanner," *IEEE Trans. Med. Img.*, vol. 13, pp. 610–618, 1994.
- [9] T. J. Spinks, D. L. Bailey, P. M. Bloomfield, et al. Performance of a new 3D-only PET scanner - the EXACT3D. *Proceedings of The IEEE Nuclear Science Symposium and Medical Imaging Conference*, pp. 1275–1279, (Edited by A. Del Guerra), Anaheim, CA, 1996.
- [10] S. R. Cherry, Y. Shao, R. W. Silverman, et al., "MicroPET: a high resolution PET scanner for imaging small animals," *IEEE Trans. Nucl. Sci.*, vol. NS-44, (in press), 1997.
- [11] R. LeComte, J. Cadorette, S. Rodrigue, et al., "Initial results from the Sherbrooke avalanche photodiode positron tomograph," *IEEE Trans. Nucl. Sci.*, vol. NS-43, pp. 1952–1957, 1996.
- [12] P. M. Bloomfield, S. Rajeswaran, T. J. Spinks, et al., "The design and physical characteristics of a small animal positron emission tomograph," *Phys. Med. Bio.*, vol. 40, pp. 1105–1126, 1995.
- [13] K. Wienhard, M. Dahlbom, L. Eriksson, et al., "The ECAT EXACT HR: performance of a new high resolution positron scanner," *J. Comp. Asst. Tomog.*, vol. 18, pp. 110–118, 1994.
- [14] W. W. Moses and S. E. Derenzo, "Empirical observation of performance degradation in positron emission tomographs utilizing block detectors," *J. Nucl. Med.*, vol. 34, pp. 101P, 1993.
- [15] S. C. Strother, M. E. Casey, and E. J. Hoffman, "Measuring PET scanner sensitivity: Relating count rates to image signal-to-noise ratios using noise equivalent counts," *IEEE Trans. Nucl. Sci.*, vol. NS-37, pp. 783–788, 1990.
- [16] T. R. DeGrado, T. G. Turkington, J. J. Williams, et al., "Performance characteristics of a whole-body PET scanner," *J. Nucl. Med.*, vol. 35, pp. 1398–1406, 1994.
- [17] C. W. Stearns, S. R. Cherry, and C. J. Thompson, "NECR analysis of 3D PET scanner designs," *IEEE Trans. Nucl. Sci.*, vol. NS-42, pp. 1075–1079, 1995.
- [18] R. A. DeKemp and C. Nahmias, "Attenuation correction in PET using single photon transmission measurement," *Med. Phys.*, vol. 21, pp. 771–778, 1994.
- [19] J. S. Karp, G. Muehllehner, H. Qu, et al., "Singles transmission in volume imaging with a Cs-137 source," *Phys. Med. Bio.*, vol. 40, pp. 929–944, 1995.
- [20] W. W. Moses, R. H. Huesman, and S. E. Derenzo, "A new algorithm for using depth-of-interaction measurement information in PET data acquisition," *J. Nucl. Med.*, vol. 32, pp. 995, 1991.
- [21] S. E. Derenzo, "Initial characterization of a BGO-silicon photodiode detector for high resolution PET," *IEEE Trans Nucl Sci.*, vol. NS-31, pp. 620–626, 1984.